

Assessing the Performances of Dispersion-Corrected Density Functional Methods for Predicting the Crystallographic Properties of High Nitrogen Energetic Salts

Dan C. Sorescu,^{†,‡} Edward F. C. Byrd,^{*,§} Betsy M. Rice,[§] and Kenneth D. Jordan^{†,‡,||}

[†]National Energy Technology Laboratory, United States Department of Energy, Pittsburgh, Pennsylvania 15236, United States

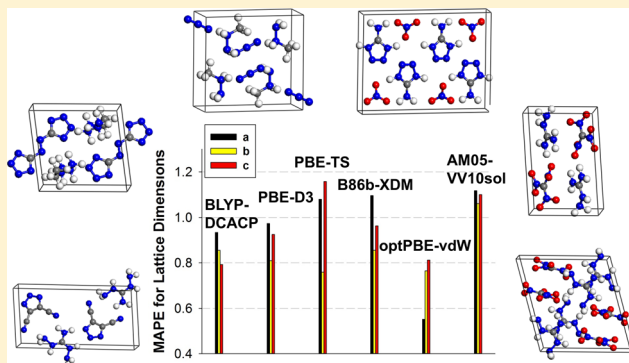
[‡]Department of Chemical and Petroleum Engineering, University of Pittsburgh, Pittsburgh, Pennsylvania 15261, United States

[§]United States Army Research Laboratory, RDRL-WML-B, Aberdeen Proving Ground, Maryland 21005-5066, United States

^{||}Department of Chemistry, University of Pittsburgh, Pittsburgh, Pennsylvania 15260, United States

S Supporting Information

ABSTRACT: Several density functional methods with corrections for long-range dispersion interactions are evaluated for their capabilities to describe the crystallographic lattice properties of a set of 26 high nitrogen-content salts relevant for energetic materials applications. Computations were done using methods that ranged from adding atom–atom dispersion corrections with environment-independent and environment-dependent coefficients, to methods that incorporate dispersion effects via dispersion-corrected atom-centered potentials (DCACP), to methods that include nonlocal corrections. Among the functionals tested, the most successful is the nonlocal optPBE-vdW functional of Klimeš and Michaelides that predicts unit cell volumes for all crystals of the reference set within the target error range of $\pm 3\%$ and gives individual lattice parameters with a mean average percent error of less than 0.81%. The DCACP, Grimme's D3, and Becke and Johnson's exchange-hole (XDM) methods, when used with the BLYP, PBE, and B86b functionals, respectively, are also quite successful at predicting the lattice parameters of the test set.



1. INTRODUCTION

The availability of accurate computational methods for materials design and assessment is critical in reducing the manpower and financial costs associated with synthesizing and testing of novel energetic materials. However, reliance on computational tools is only warranted if they possess sufficient accuracy in predicting the desired properties. One such property, the crystalline density, is of particular importance in predicting the performances of energetic materials. While different methods exist for predicting crystal densities, many do not exhibit the desired accuracy with error of 3% or less in the density.¹ As is well known, first-principles density functional theory (DFT)^{2,3} methods tend to perform poorly for molecular crystals for which van der Waals (vdW) interactions provide a significant contribution to the overall binding.^{1,4} The inability to describe long-range dispersion interactions has long been recognized as one of the most serious deficiencies in common DFT methods. Several different strategies for correcting DFT for long-range dispersion interactions have been developed,^{5–9} and all of these lead to improved predictions of the structures and cohesive energies of molecular crystals.^{7,8,10}

In a recent review, Klimeš and Michaelides⁶ provided a general classification of various methods that have been developed to correct DFT for dispersion interactions. In this

classification, the first group of methods improves the description of dispersion at intermediate distances while falling off more rapidly than R^{-6} at long-range. These include the dispersion-corrected atom-centered potentials (DCACP) method of Rothlisberger and co-workers⁹ and the Minnesota functionals developed in Truhlar group.^{11,12} In the former, parameters in the pseudopotentials were fit so as to closely reproduce the interaction energies from high-level ab initio calculations on selected dimers, and in the latter, parameters in the functionals were fit to best predict a wide range of energetic properties, including ionization potentials, electron affinities, and atomization energies. We note that in the case of the DCACP method, performance at large interatomic separations can be significantly improved by including additional channels in the atom-centered potentials.¹³ A previous study of energetic materials using the DCACP method has shown greatly improved predictions of crystallographic parameters over those obtained using uncorrected DFT methods.¹⁰

A second class of methods for correcting DFT for missing dispersion interactions involves adding a correction to the energy of the form^{14,15}

Received: July 1, 2014

$$E_{\text{disp}} = \sum_{B>A} \sum_{n=6,8,10} s_n \frac{C_n^{\text{AB}}}{R_{\text{AB}}^n} f_n(R_{\text{AB}}) \quad (1)$$

where the sum runs over the atomic sites A and B , C_6^{AB} , C_8^{AB} , and C_{10}^{AB} are dispersion coefficients for the atomic pair (AB) , f_n is a damping function which prevents double counting of dispersion interactions in the overlap regions and damps out the dispersion interactions at short R_{AB} separations, and the s_n are global functional-dependent scaling factors.

In Grimme's DFT-D2 method,¹⁴ only the $n = 6$ terms in eq 1 are included and the C_6 parameters for pairs of atoms with the same atomic number are fixed and are determined from atomic polarizabilities and ionization energies, while the C_6 coefficients between unlike atoms are determined using the geometric mean. The damping parameter is only functional dependent. Although this approach neglects the dependence of the C_6^{AB} coefficients on the chemical environment and does not explicitly account for the R^{-8} or R^{-10} dispersion contributions, it has been found to significantly improve the properties of molecular crystals compared to the results of uncorrected DFT methods.^{16,17} In particular, for a group of 15 molecular crystals containing different nitramines, nitroalkanes, nitroaromatics, nitrocubanes, nitrate esters, and amino-nitro derivatives, including the RDX, HMX, PETN, TATB, TNT, and FOX-7 energetic materials, the DFT-D2 values of the lattice parameters (unit cell volumes) at ambient pressure and under hydrostatic compression conditions were found to be within 2% (3%) of the corresponding experimental values in all but two cases.¹⁸ However, tests that we carried out on a series of ionic crystals (discussed below) revealed that the DFT-D2 is much less successful at predicting the structures of these crystals.

In order to obtain more accurate structures of molecular crystals, it is necessary to use a scheme in which the dispersion-correction depends on the chemical environment. Methods that employ environment-dependent C_6/R^6 corrections in the general form of eq 1 include the DFT-D3 method of Grimme et al.,¹⁹ the vdW-TS approach of Tkatchenko and Scheffler,²⁰ and the exchange-hole model of Becke and Johnson.^{21–23}

In the DFT-D3 method,¹⁹ the environmental dependence of the dispersion corrections is included by considering fractional coordination numbers determined from the number of neighbors of each atom. The method also includes C_8/R^8 terms. In addition to being implemented with the BLYP and PBE functionals, it can also be used with the B97-D¹⁴ or ω B97X-D²⁴ methods, which have been designed and explicitly parametrized for this purpose. The DFT-D3 method allows for the optional inclusion of three-body dispersion corrections.^{15,19,25}

In the vdW-TS method,²⁰ environment-dependent C_6 coefficients are obtained by using frequency-dependent polarizabilities of the free atoms scaled by ratios of the effective and free volumes. The effective volumes are obtained by partitioning the electron density in the molecule or in the solid by using Hirshfeld partitioning.²⁶ The original TS method²⁰ has been extended to include self-consistent screening (denoted as TS+SCS) and many-body effects (denoted as TS+MBD).²⁷

In the XDM method,^{21–23,28,29} C_6 , C_8 , and C_{10} coefficients for interactions between atomic pairs are estimated from the averages of the square of the atomic moments $\langle m_i^2 \rangle$, calculated using atomic polarizabilities determined using Hirshfeld partitioning. The XDM correction is generally combined with

a DFT exchange functional such as Becke86 (B86b)³⁰ or Perdew–Wang86 (PW86)³¹ that closely reproduces Hartree–Fock repulsive interactions. This approach has been demonstrated to be highly successful in predicting noncovalent interactions in solids.⁷

As noted above, a common characteristic of the Grimme, TS, and Becke–Johnson approaches is the use of a damping function to eliminate unphysical contributions at short separations. In general, the parameters in the damping function are obtained by fitting high-level ab initio results for molecular dimers, and as a result, in addition to correcting for dispersion interactions, these methods may also be correcting for other DFT deficiencies.³²

An alternative approach to correcting DFT for dispersion involves adding a nonlocal correlation term to the local or semilocal correlation functional. In the original formulation of this approach introduced by Dion et al.,³³ called van der Waals density functional (vdW-DF), a nonlocal term of the form

$$E_{\text{C}}^{\text{NL}} = \frac{1}{2} \iint \rho(\mathbf{r}) \Phi(\mathbf{r}, \mathbf{r}') \rho(\mathbf{r}') d^3r d^3r' \quad (2)$$

is added to the exchange-correlation energy, $E_{\text{xc}} = E_{\text{x}}^{\text{GGA}} + E_{\text{c}}^{\text{LDA}} + E_{\text{c}}^{\text{NL}}$. In eq 2, $\rho(\mathbf{r})$ is the electron density at position \mathbf{r} and $\Phi(\mathbf{r}, \mathbf{r}')$ is a correlation kernel that depends on the electron density and its gradient at \mathbf{r} and \mathbf{r}' .³³ $E_{\text{c}}^{\text{LDA}}$ describes the short-range correlation effects, while E_{c}^{NL} term describes the long-range dispersion. The vdW-DF functional has been shown to provide clear improvements relative to standard functionals for describing dispersion interactions; however, it tends to overestimate the dispersion contribution at long-range.^{34–36} This limitation was partially addressed in a second generation approach, called vdW-DF2^{34,35} which improves the description of the interaction energies of weakly bound systems near their potential energy minima but, in general, does not give accurate values for the C_6 coefficients.³⁷ Recently, the Michaelides group examined the performance of the vdW-DF method when used with different exchange functionals and introduced the optB88-vdW, optB86b-vdW, and optPBE-vdW functionals,^{38,39} which were found to perform well for both finite³⁸ and extended systems.³⁹

Vydrov and Van Voorhis have introduced the VV09³⁶ and VV10⁴⁰ nonlocal functionals. The more recent VV10 functional combines the nonlocal $E_{\text{c}}^{\text{VV10}}$ functional with the refitted PW86 (rPW86) exchange functional and the PBE correlation functional, $E_{\text{xc}}^{\text{VV10}} = E_{\text{x}}^{\text{rPW86}} + E_{\text{c}}^{\text{PBE}} + E_{\text{c}}^{\text{VV10}}$.⁴⁰ In general, the VV10 functional performs better than VDW-DF or VDW-DF2 in describing weakly interacting systems.^{40,41} However, when applied to solids the VV10 functional tends to overestimate the binding energies and the elastic coefficients of layered compounds.⁴² Björkman⁴³ has addressed these limitations by refitting two parameters of the VV10 functional leading to the PW86R-VV10sol functional⁴⁰ as well as by introducing a new functional, denoted AM05-VV10sol, which combines the modified nonlocal correlation functional VV10sol with the generalized gradient functional of Armiento and Mattson (AM05).⁴⁴ The AM05-VV10sol functional has been found to give accurate structures of both weakly bonded systems and close packed solids.⁴³

In this paper, we analyze the performance of several uncorrected and dispersion-corrected functionals at predicting the crystal lattice parameters for a set of 26 high nitrogen content energetic salts hereafter denoted as the S26 set. These materials are of considerable interest due to their high heats of

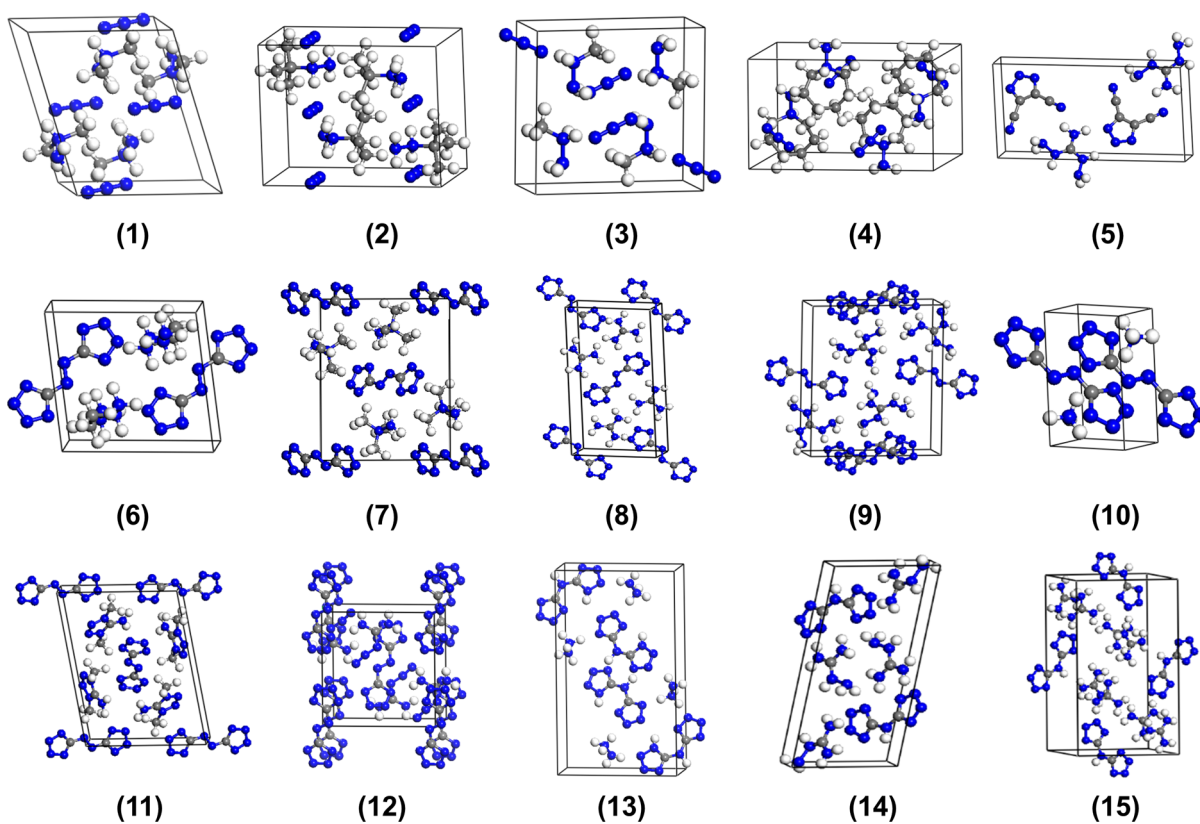


Figure 1. Pictorial view of the high nitrogen content molecular salts investigated in this work. The crystal numbering scheme follows that used in Table 1.

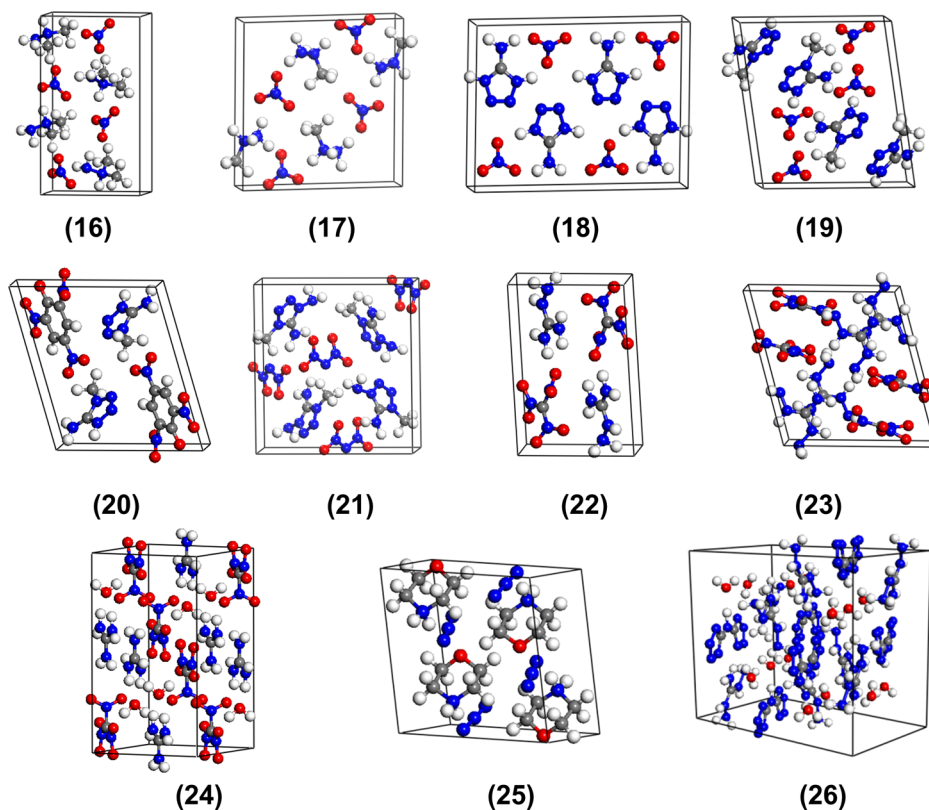


Figure 2. Pictorial view of the C–N–O–H subset of high molecular salts investigated in this work. For each case the indicated index label is detailed in Table 1.

Table 1. List of the S26 Set of High Nitrogen Salts Investigated in this Work^a

compd. ^b (chem. formula)	space group, <i>Z</i> ^c	<i>a</i> (Å)	<i>b</i> (Å)	<i>c</i> (Å)	α (deg.)	β (deg.)	γ (deg.)	vol. (Å ³)
(1) 1,1-dimethylhydrazinium azide (C ₂ H ₉ N ₃) ⁴⁹	<i>P2₁/n</i> , <i>Z</i> = 4	8.4451	7.0415	10.0748	90.00	108.321	90.00	568.74
(2) <i>tert</i> -butylhydrazinium azide (C ₄ H ₁₃ N ₃) ⁵⁰	<i>Pbcm</i> , <i>Z</i> = 4	6.9234	12.1203	9.5133	90.00	90.00	90.00	798.30
(3) methylhydrazinium azide (CH ₇ N ₃) ⁵¹	<i>Pnma</i> , <i>Z</i> = 4	9.962	5.1316	9.228	90.00	90.00	90.00	471.77
(4) N-amino-1-azoniacyclo-heptane azide (C ₆ H ₁₅ N ₃) ⁵²	<i>P2₁/c</i> , <i>Z</i> = 4	7.7694	8.2459	13.866	90.00	99.72	90.00	875.50
(5) diaminoguanidinium 4,5-dicyano-1,2,3-triazolate (C ₅ H ₈ N ₁₀) ⁵³	<i>P2₁</i> , <i>Z</i> = 2	3.7727	15.6832	8.3416	90.00	101.797	90.00	483.13
(6) ethylenedihydrazinium(2+) 5,5'-azotetrazolate (C ₄ H ₁₂ N ₁₄) ⁵⁴	<i>P$\bar{1}$</i> , <i>Z</i> = 2	7.4364	8.5200	9.2620	97.818	102.113	91.528	567.50
(7) bis(N,N,N-trimethyl-hydrazinium) 5,5'-azotetra-zolate (C ₈ H ₂₂ N ₁₄) ⁵⁵	<i>P2₁/n</i> , <i>Z</i> = 2	5.7003	13.1862	10.6737	90.00	101.453	90.00	786.33
(8) diguanidinium 5,5'-azotetrazolate (C ₄ H ₁₂ N ₁₆) ⁵⁴	<i>P2₁/c</i> , <i>Z</i> = 2	3.6155	17.754	9.3800	90.00	91.63	90.00	601.84
(9) bis-triaminoguanidinium 5,5'-azotetrazolate (C ₄ H ₁₈ N ₂₂) ⁵⁴	<i>P2₁/n</i> , <i>Z</i> = 2	3.9155	15.014	12.995	90.00	95.031	90.00	761.01
(10) diammonium 5,5'-azotetrazolate (C ₂ H ₈ N ₁₂) ⁵⁵	<i>P$\bar{1}$</i> , <i>Z</i> = 1	4.3095	7.265	7.366	73.53	77.17	77.65	212.79
(11) bis(1,4-dimethyl-5-aminotetrazolium) 5,5'-azotetrazolate (C ₈ H ₁₆ N ₂₀) ⁵⁶	<i>P$\bar{1}$</i> , <i>Z</i> = 2	5.830	10.994	14.706	99.93	93.64	98.72	913.82
(12) bis-azidoformamidinium 5,5'-azotetrazolate (C ₄ H ₈ N ₂₀) ⁵⁷	<i>P2₁/n</i> , <i>Z</i> = 2	9.928	6.9088	10.026	90.00	90.16	90.00	687.65
(13) bis-hydrazine 5,5'-bis(tetrazolyl)amine (C ₂ H ₇ N ₁₁) ⁵⁸	<i>P2₁/c</i> , <i>Z</i> = 4	3.6473	10.9312	18.2745	90.00	95.481	90.00	725.26
(14) bis-aminoguanidinium 5,5'-bis(tetrazolyl)amine (C ₄ H ₁₅ N ₁₇) ⁵⁸	<i>P$\bar{1}$</i> , <i>Z</i> = 2	5.4155	7.3337	15.875	97.78	97.77	97.70	611.47
(15) bis(guanidinium)bis(tetrazolato)amine (C ₄ H ₁₃ N ₁₅) ⁵⁸	<i>P2₁/c</i> , <i>Z</i> = 4	7.0918	17.7986	9.6724	90.00	109.68	90.00	1149.53
(16) N,N-dimethylhydrazinium nitrate (C ₂ H ₉ N ₃ O ₃) ⁵⁹	<i>Pna2₁</i> , <i>Z</i> = 4	14.0388	5.6493	7.6026	90.00	90.00	90.00	602.96
(17) methylhydrazinium nitrate (CH ₇ N ₃ O ₃) ⁵⁹	<i>P2₁/c</i> , <i>Z</i> = 4	3.7794	11.342	11.107	90.00	99.09	90.00	470.14
(18) 5-aminotetrazolium nitrate (CH ₄ N ₆ O ₃) ⁶⁰	<i>P2₁/c</i> , <i>Z</i> = 4	10.5493	3.4556	14.606	90.00	90.584	90.00	532.44
(19) 1-methyl-5-aminotetrazolium nitrate (C ₂ H ₆ N ₅ ⁺ NO ₃ ⁻) ⁶¹	<i>P2₁/n</i> , <i>Z</i> = 4	10.6122	5.3606	11.5508	90.00	97.663	90.00	651.23
(20) 5-amino-1-methyl-1H-tetrazolium picrate (C ₈ H ₈ N ₈ O ₇) ⁶²	<i>P$\bar{1}$</i> , <i>Z</i> = 2	5.895	10.126	11.578	106.96	100.88	98.02	635.17
(21) 1,5-diamino-4-methyl-1H-tetrazolium dinitramide (C ₂ H ₇ N ₉ O ₄) ⁶³	<i>P2₁2₁2₁</i> , <i>Z</i> = 4	5.2632	12.3766	13.1225	90	90	90	854.81
(22) aminoguanidinium nitroformate (C ₂ H ₇ N ₇ O ₆) ⁶⁴	<i>P$\bar{1}$</i> , <i>Z</i> = 2	5.0690	7.5590	11.320	84.567	84.425	79.609	423.29
(23) diaminoguanidinium nitroformate (C ₂ H ₈ N ₈ O ₆) ⁶⁴	<i>P2₁/n</i> , <i>Z</i> = 4	10.980	7.7524	11.415	90.00	105.336	90.00	937.13
(24) guanidinium nitroformate monohydrate (C ₂ H ₆ N ₆ O ₆ ·H ₂ O) ⁶⁴	<i>C2/c</i> , <i>Z</i> = 4	8.1859	14.3541	7.7556	90.00	101.132	90.00	894.15
(25) 1-azonia-4-oxacyclo-hexane (C ₄ H ₁₀ N ₄ O) ⁶²	<i>P2₁/n</i> , <i>Z</i> = 4	6.998	9.473	10.171	90.00	107.982	90.00	641.27
(26) bis(diaminoguanidine) iminobis (5-tetrazolate) (C ₄ H ₂₃ N ₁₉ O ₃ ·3H ₂ O) ⁶⁵	<i>C2/c</i> , <i>Z</i> = 4	8.5514	13.3343	14.9890	90	97.589	90	1694.18

^aFor each crystal the corresponding space group, lattice vectors and lattice angles are indicated. ^bAll crystallographic measurements were taken at *T* = 200 K except in the following cases: (2) (*T* = 183 K), (9) (*T* = 193 K), (12) (*T* = 295 K), and (26) (*T* = 90 K). ^c*Z* indicates the number of formula units per unit cell.

formation and high densities.^{45–48} They are prime candidates for “green” energetic material applications since a major product of their combustion is molecular nitrogen.

The S26 test set includes crystals with different types of C–N–H (see Figure 1) and C–N–O–H (see Figure 2) compositions, spanning different chemical groups and functionalities. The C–N–H list includes crystals containing different types of azide,^{49–52} dicyano-triazolate,⁵³ 5,5'-azotetrazolate,^{54–57} and 5,5'-bis(tetrazolyl)-amine⁵⁸ anions, while the C–N–O–H set includes crystals containing combinations of nitrate cations with different hydrazinium⁵⁹ and amino-tetrazolium^{60,61} anions as well as systems containing picrate,⁶² dinitramide,⁶³ nitroformate,⁶⁴ and azide⁵² anions or the hydrated form of bis(diaminoguanidine) iminobis(5-tetrazolate).⁶⁵ These systems have been synthesized and characterized by X-ray diffraction methods in the groups of Klapeetke^{49–64} and Shreeve.⁶⁵ The full list of compounds and their experimental crystallographic parameters are given in Table 1. Schematic representation of the corresponding pairs of cations and anions for each of the crystals analyzed is presented in Schemes S1 and S2 in the Supporting Information.

2. COMPUTATIONAL METHODS

Optimization of the S26 set of structures was done using the Quickstep module⁶⁶ of the CP2K program,⁶⁷ and the VASP^{68,69} and Quantum Espresso⁷⁰ codes. The use of three different codes was necessary as only a subset of the examined dispersion-correction schemes is implemented in each code. The Quickstep code uses a mixed Gaussian and plane-wave formalism⁷¹ and the VASP^{68,69} and Quantum Espresso⁷⁰ codes use plane-wave basis sets. In all instances, cells with 3D periodic boundary conditions were used to represent the bulk structure of the crystals of interest.

The Quickstep code was used to carry out calculations using the PBE⁷² and BLYP^{73,74} functionals both without dispersion corrections and with the DCACP,⁹ D2,¹⁴ and D3¹⁹ corrections for dispersion. In the following discussion, we indicate the combination of functional and dispersion correction with the acronyms DCACP-PBE (or DCACP-BLYP), PBE-D2 (or BLYP-D2), and PBE-D3 (or BLYP-D3). In the case of the PBE-D3 functional, calculations were also carried out including three-body dispersion corrections as described in ref 15 with the method hereafter denoted as PBE-D3-C9. For comparison, we have also included results obtained using the dispersion-corrected revPBE-D3⁷⁵ and B97D-D¹⁴ functionals.

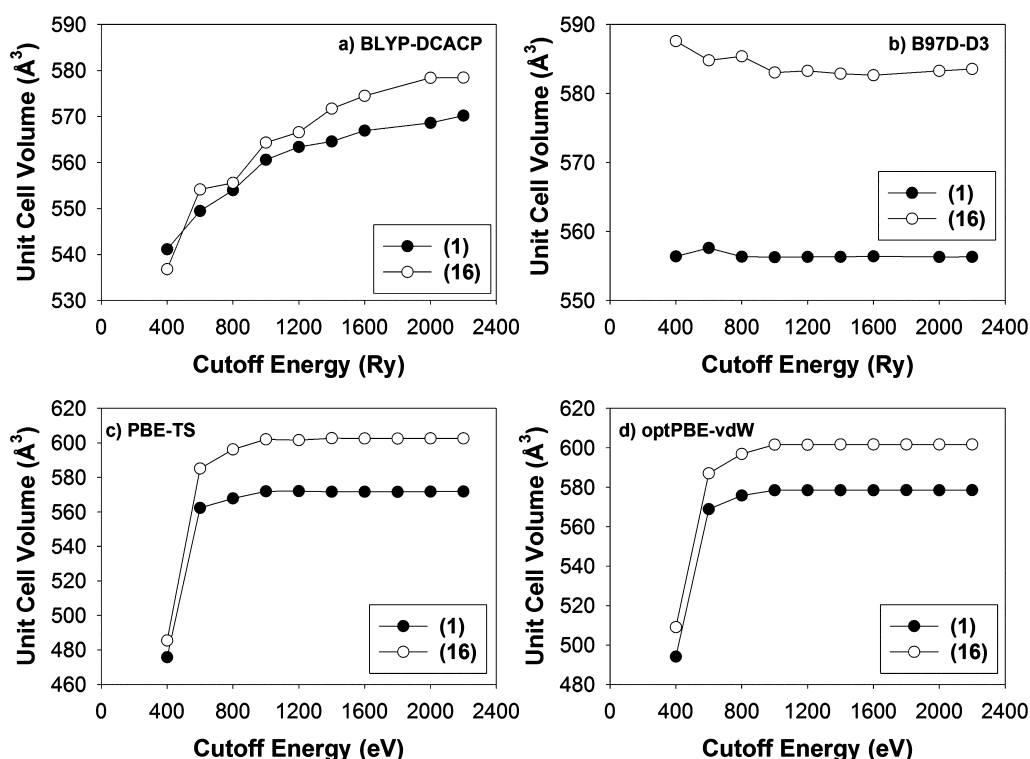


Figure 3. Variation of the unit cell volume with cutoff energy calculated using (a) BLYP-DCACP, (b) B97D-D3, (c) PBE-TS, and (d) optPBE-vdW functionals for the molecular crystals (1) and (16). Calculations were performed using CP2K (a, b) and VASP (c, d) codes, respectively.

The calculations with the TS dispersion correction and with the nonlocal functionals were performed using the VASP code. The TS correction was used in conjunction with the PBE functional (hereafter this approach is denoted as PBE-TS²⁰). In addition, calculations were also carried out with the TS scheme including self-consistent screening (PBE-TS+SCS) method²⁷ to account for electrodynamic response effects. These methods were recently implemented in VASP code by Bučko et al.⁷⁶

The nonlocal van der Waals functionals considered include the revised vdW-DF2 method of Langreth–Lundqvist,³⁵ the optB88-vdW, optB86b-vdW, and optPBE-vdW functionals of Klimeš et al.,^{38,39} and the AM05-VV10sol functional of Armiento and Mattson (AM05)⁴⁴ modified by Björkman.⁴³ With the exception of AM05-VV10sol, these calculations were performed using VASP; the AM05-VV10sol calculations were performed using the CP2K code.⁶⁷ For this purpose, we made use of AM05 functional as implemented in the LIBXC library⁷⁷ while for the nonlocal dispersion functional we used the modified version of the VV10 functional as described in ref 43.

The implementation of the VV10 nonlocal term in CP2K is based on the method of Sabatini et al.⁷⁸ to evaluate the nonlocal correlation energy and its derivatives in a plane-wave framework along with the scheme of Román-Pérez and Soler⁷⁹ to factorize the integration kernel and using fast Fourier transforms to evaluate the self-consistent energy in $O(N \log N)$ operations.

All CP2K calculations were performed using the Gaussian triple- ζ valence TZV2P basis sets⁸⁰ with two sets of polarization functions and a plane-wave cutoff of 2000 Ry for the electronic density. Norm-conserving Goedecker, Teter, and Hutter (GTH) pseudopotentials⁸¹ were used to represent the core electrons in the calculations using CP2K. In each calculation, a full-dimensional variable cell optimization at ambient pressure using an analytical stress tensor was performed using the

conjugate gradient (CG) method for optimizing the cell degrees of freedom and Broyden–Fletcher–Goldfarb–Shanno (BFGS) optimizer was used for the ionic degrees of freedom. As CP2K is a gamma-point only code, calculations were performed using a supercell composed of multiple unit cells. The $N_1 \times N_2 \times N_3$ sets of unit cells considered in calculations for each individual crystal are indicated in Table S3 in the Supporting Information.

In the calculations using VASP the electron–ion interactions were described by the projector augmented wave (PAW) method of Blöchl⁸² in the implementation of Kresse and Joubert.⁸³ A cutoff energy of 1000 eV was used for the plane-wave basis set expansion. Brillouin zone sampling was obtained using a Monkhorst–Pack⁸⁴ set of k-points, which permitted the use of the unit cell as the supercell. As k-point sampling is allowed in VASP, these calculations were limited to a single unit cell. The specific k-point grid ($K_1 \times K_2 \times K_3$) for each crystal analyzed is indicated in the Supporting Information Table S4. Crystal optimizations were done by relaxing the lattice dimensions and angles as well as the atomic positions to minimize the stress tensor.

The calculations with the XDM-corrected functional of Becke and Johnson²³ were carried out using Otero-de-la-Roza and Johnson's implementation^{28,85} in the Quantum Espresso code.⁷⁰ Specifically, we used the XDM dispersion correction with the B86b exchange³⁰ and PBE correlation⁷² functionals (hereafter denoted as B86b-XDM). In the present calculations using this method, the electron–ion interactions were represented using the PAW method of Blöchl.⁸² A kinetic energy cutoff of 80 Ry was used for the orbitals. The Monkhorst–Pack sets of k-points used for the various crystals were the same as those used in the VASP calculations (see Supporting Information Table S4). For all calculations (CP2K, VASP, and Quantum Espresso), the initial configurations of

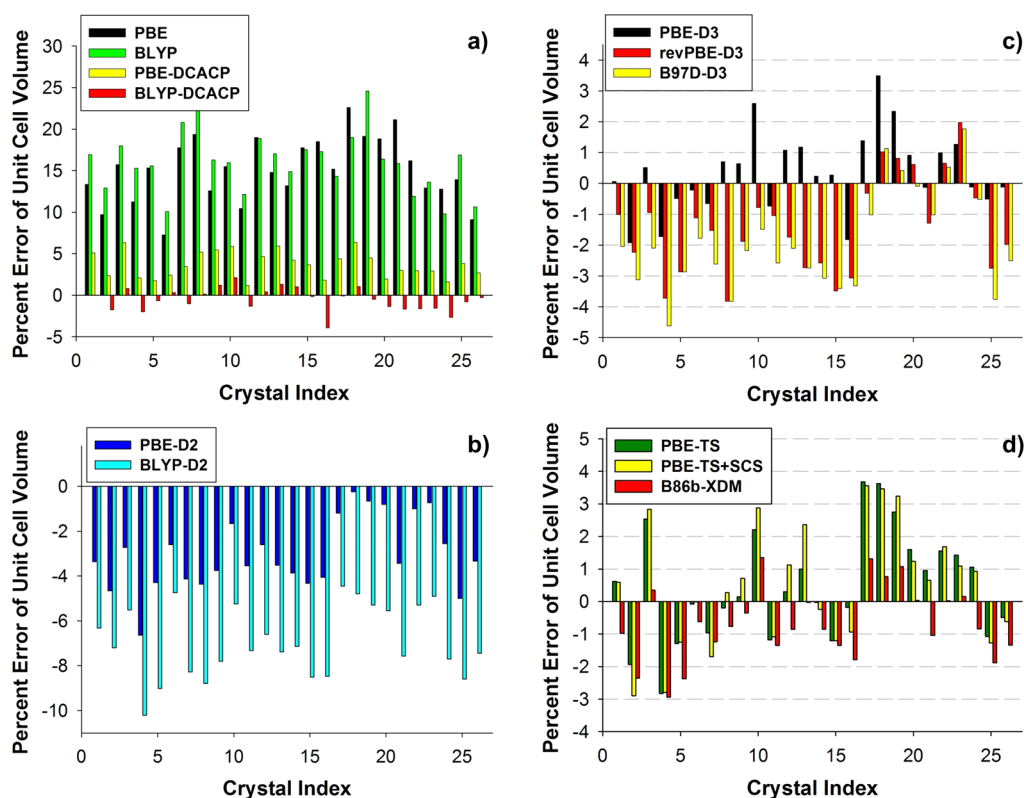


Figure 4. Variation of the percent error of the calculated unit cell volumes relative to experimental values for the S26 set as determined using the following methods: (a) PBE, BLYP, PBE-DCACP, and BLYP-DCACP; (b) PBE-D2 and BLYP-D2; (c) PBE-D3, revPBE-D3, and B97D-D3; and (d) PBE-TS, PBE-TS+SCF, and B86b-XDM.

each system was taken to correspond to the experimental crystal structure.

The choice of the plane-wave cutoff energies of 2000 Ry in CP2K, 1000 eV in VASP and 80 Ry in Quantum Espresso warrants additional comments. First, we report the cutoffs for each code in the default units of that code. Second, in the case of CP2K, the cutoff is for the charge density expansion, while for VASP and Quantum Espresso, the indicated cutoffs are for the orbital energies. The convergence of the optimized unit cell volume with increasing cutoff energy was checked for each method with the results being illustrated in Figure 3. Panels a and b in this figure report the results for the DCACP and B97D-D3 calculations performed using CP2K, while the bottom two panels report the results for the PBE-TS and optPBE-vdW calculations using the VASP code. The tests were performed for crystals arbitrary selected from the C–N–H set, that is, crystal (1), and from the C–N–O–H set, that is, crystal (16).

As seen from Figure 3a, with the DCACP calculations performed using CP2K, convergence is only approximately reached even at plane-wave cutoffs as high as 2000 Ry. The need to use such large cutoff energies in DCACP calculations with CP2K was noted in a previous study of bulk optimization of neutral nitramine crystals.¹⁰ For the PBE-D2, PBE-D3, revPBE-D3, and B97D-D3 calculations, using CP2K convergence is reached at cutoff energies of about 1000 Ry for the density as shown in Figure 3b for the case of B97D-D3. However, for consistency a cutoff energy of 2000 Ry was used in all CP2K calculations.

Similarly, we evaluated the convergence dependence of unit cell volumes for crystals (1) and (16) when using the B86b-

XDM method as implemented in Quantum Espresso, with the results being reported in Figure S9 in the Supporting Information. For these crystals, convergence of the predicted unit cell volumes was obtained at a kinetic energy cutoff of about 70 Ry. Based on this result, a cutoff of 80 Ry was chosen for all calculations using the XDM method.

For the PBE-TS and optPBE-vdW calculations performed using the VASP code, the results indicated in panels c and d of Figure 3 demonstrate that convergence is reached for plane-wave cutoff energies of about 1000 eV. As a result, all subsequent calculations using VASP employed a cutoff of 1000 eV. Using the computational conditions described above, we find that the lattice constants obtained using the same functional but implemented in different codes are very close to each other. This is shown in Figure S10 in the Supporting Information section where we compare the unit cell volumes for the S26 set calculated using the PBE-D3 method as implemented in VASP and CP2K codes.

3. RESULTS AND DISCUSSION

In this section, we analyze the cell volume and lattice constants obtained using the uncorrected and dispersion-corrected DFT methods discussed above. Figure 4a indicates the percent errors of the unit cell volume of the S26 set of ionic salt crystals calculated using the PBE, BLYP, DCACP-PBE, and DCACP-BLYP exchange-correlation functionals. As expected, both the calculations with the PBE and BLYP functionals greatly overestimate the unit cell volumes of the crystals, with the errors being 7–22% (9–25%) for PBE (BLYP) functionals.

Significantly improved results are obtained with the DCACP corrected functionals. In the case of PBE-DCACP, the unit cell

volumes are overestimated by 1.2–6.0%, while for BLYP-DCACP the errors in the volumes range from −3.9 to 2.1%. In fact, excluding (16), the DCACP-BLYP method gives unit cell volumes within the target error of $\pm 3\%$ from the experimental values. Clearly, the BLYP-DCACP method is quite successful at predicting the unit cell volumes for the S26 set of crystals.

The results of the PBE-D2 and BLYP-D2 calculations are reported in Figure 4b. Of these two approaches, the PBE-D2 method is more successful at predicting the crystal volumes with the errors ranging from −6.6% to −0.2% as compared with the −10.2% to −4.4% errors for BLYP-D2. Even for PBE-D2, the calculated volumes for over half of the crystals are outside the target error range of 3%.

Figure 4c and d summarize the volumes obtained with methods employing environment-dependent C_6/R^6 corrections. These include using the D3 method in conjunction with the PBE, BLYP, revPBE, and B97D functionals and the TS scheme in combination with the PBE functional. The BLYP-D3 method proved to be less accurate than the other DFT-D3 methods while the PBE-D3-C9 results are similar in accuracy to revPBE results, and, for simplicity of visualization, were not included in Figure 4c (the data are included in Supporting Information Table S5).

For the DFT-D3 methods the percent errors for the unit cell volumes are in the range (−1.9, 3.5)% for PBE-D3, (−0.7, 4.8)% for PBE-D3-C9, (−7.4, −2.6)% for BLYP-D3, (−3.8, 1.9)% for revPBE-D3, and (−4.6, 1.8)% for B97D-D3. Of these approaches, PBE-D3 and revPBE-D3 lead to volumes that are closest to the experimental values, missing the target error value of $\pm 3\%$ for only one and four cases, respectively. We note that the largest error obtained with the PBE-D3 method is for crystal (18) 5-aminotetrazolium nitrate. As will be seen below, this crystal is also a problem case for the PBE-TS and PBE-TS+SCF functionals. With the PBE-TS approach, the errors in the volumes range from −2.8 to 3.7%. The inclusion of the self-consistent screening (TS+SCS) does not systematically improve the calculated unit cell volumes, with the percent error deviations increasing slightly relative to those from the TS method. The largest errors in the calculated volumes are found for crystals (17) and (18), the latter also being the system giving the largest error for PBE-D3 method.

The final method considered that adds a correction of the form of eq 1 is B86b-XDM. For this method, the percent errors of the predicted unit cell volume are in the range (−2.9, 1.3)%. Overall, the PBE-D3, PBE-TS, and B86b-XDM provide similar results for the unit cell volumes, with relatively narrow spreads around zero percent error. In particular, for the B86b-XDM method, the calculated volume is within the target range, while there are one and respectively two exceptions for PBE-D3 and PBE-TS, respectively.

The final approaches considered were the optB88-vdW, optB86b-vdW, optPBE-vdW, vdW-DF2, and AM05-VV10sol nonlocal functionals.^{35,38,43} The performance of these nonlocal correlation functionals for predicting the unit cell volumes of the S26 set is reported in Figure 5.

The optB88-vdW and optB86b-vdW methods underestimate the unit cell volumes and have similar error distributions, namely, (−4.5, −1.1)% and (−4.1, −1.2)%, respectively. In contrast the vdW-DF2 functional overestimates the experimental unit cell volumes by values ranging from 0.4 to 4.8%. The best overall agreement with the experimental data is obtained with the optPBE-vdW and AM05-VV10sol functionals, for which the relative errors are distributed in the

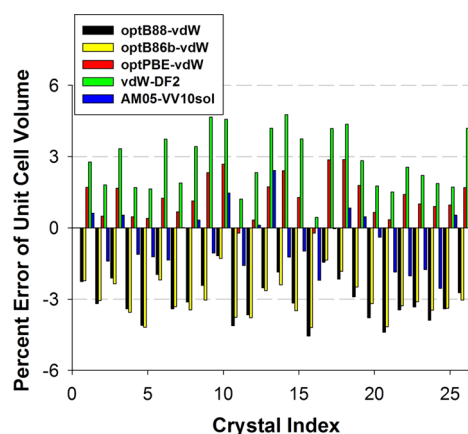


Figure 5. Variation of the percent error of the calculated unit cell volumes relative to experimental values for the S26 set using the optB88-vdW, optB86b-vdW, optPBE-vdW, vdW-DF2, and AM05-VV10sol nonlocal functionals.

ranges (−0.2, 2.8)% and (−2.5, 2.4)%, respectively. Of the functionals in this group, the optPBE-vdW functional is overall the most successful at predicting the unit cell volumes of the S26 test set.

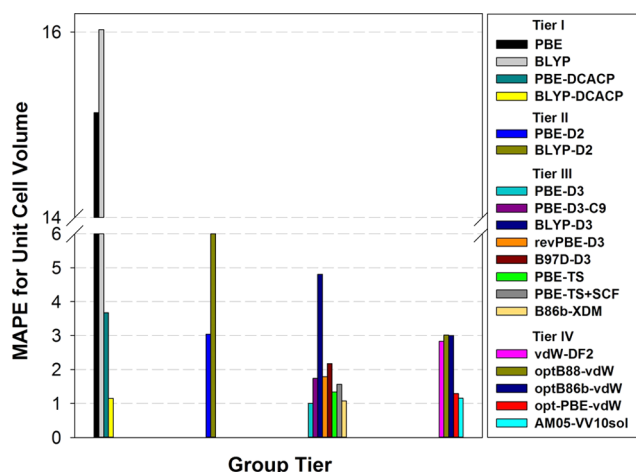
Table 2 summarizes the performance of the various DFT methods at predicting the cell volumes. Specifically, the table reports the number of crystals with predicted absolute errors distributed in bin intervals from zero to 5% using steps of 1%, as well as indicating the number of crystals with absolute errors larger than 5%. The last two columns in Table 2 sum the frequencies into two bins, one from 0 to 3% and the second one containing absolute errors larger than 3%. As mentioned above, the optPBE-vdW, AM05-VV10sol, and B86b-XDM functionals are successful in predicting the crystal volumes within the target range of $\pm 3\%$ error for the entire set of S26 crystals, while the PBE-D3 and BLYP-DCACP functionals have one missed crystal, and PBE-TS has two missed cases. The other methods considered are appreciably less successful at predicting the volumes of the S26 set of crystals.

Another metric in assessing the overall performance of the various functionals is provided by the mean absolute percentage errors (MAPE) of the predicted unit cell volumes for the S26 data set, as reported in Figure 6. Based on results in this figure several conclusions can be drawn. First, both the standard PBE and BLYP functionals are inadequate for predicting unit cell volumes, even when dealing with ionic salts materials. Second, although the DCACP method performs significantly better with the BLYP than with the PBE functional, the DFT-D2 and DFT-D3 methods perform better when used with the PBE than with the BLYP functional. Third, methods that include environment-dependent dispersion corrections are more successful at predicting the unit cell volumes of the S26 set than are the D2 methods that use fixed dispersion coefficients. The PBE-D3, revPBE-D3, vdW-TS, and B86b-XDM methods in particular are much more successful at predicting the volumes than are the PBE-D2 or BLYP-D2 methods. Neither inclusion of three-body dispersion (via PBE-D3-C9) nor allowing for self-consistent screening in the TS approach leads to significant improvements in the calculated volumes. Finally, comparison of the MAPE results indicates that the PBE-D3 and B86b-XDM, and BLYP-DCACP methods are almost as successful as the optPBE-vdW and AM05-VV10sol methods at predicting the unit cell volumes.

Table 2. Percentage Absolute Error Distribution of the Calculated Unit Cell Volumes for the S26 Set Obtained Using Different Theoretical Levels^a

method	percent error distribution						sum distributions	
	0–1%	1–2%	2–3%	3–4%	4–5%	>5%	0–3%	>3%
PBE	0	0	0	0	0	26	0	26
BLYP	0	0	0	0	0	26	0	26
PBE-DCACP	0	5	7	3	4	7	12	14
BLYP-DCACP	12	11	2	1	0	0	25	1
PBE-D2	4	3	4	7	6	2	11	15
BLYP-D2	0	0	0	0	4	22	0	26
PBE-D3	16	7	2	1	0	0	25	1
PBE-D3-C9	7	9	7	2	1	0	23	3
BLYP-D3	0	0	2	5	8	11	2	24
revPBE-D3	7	10	5	4	0	0	22	4
B97D-D3	4	6	9	6	1	0	19	7
PBE-TS	11	9	4	2	0	0	24	2
PBE-TS-SCS	9	9	5	3	0	0	23	3
B86b-XDM	13	10	3	0	0	0	26	0
vdW-DF2	1	9	5	4	7	0	15	11
optB88-vdW	0	4	7	11	4	0	11	15
optB86b-vdW	0	3	6	14	3	0	9	17
optPBE-vdW	11	10	5	0	0	0	26	0
AM05-VV10sol	11	11	4	0	0	0	26	0

^aThe final two columns indicate the total number of crystals having their unit cell volumes predicted within the desired 3% accuracy, respectively, with errors larger than this value.

**Figure 6.** Variation of the mean absolute percent error (MAPE) of the calculated unit cell volume relative to experimental data obtained using different theoretical methods considered in this study.

Since it is possible for a calculation to predict a cell volume close to experiment while having large errors in the individual lattice constants, the lattice constants provide a more stringent test of the various DFT methods than do the unit cell volumes. The RMS and MAPE errors for the calculated lattice constants are summarized in Supporting Information Tables S6 and S7. The MAPE of the lattice vectors and lattice angles for the top six most promising functionals (BLYP-DCACP, PBE-D3, PBE-TS, B86b-XDM, optPBE-vdW, and AM05-VV10sol) as determined earlier in this section are compared in Figure 7. As seen in this figure and also from the data in Table S6, of the entire set of functionals considered the optPBE-vdW method yields the lowest overall mean absolute percentage errors for individual lattice lengths followed closely by BLYP-DCACP and PBE-D3. For these three functionals, the MAPEs of the

lattice vectors range from 0.55 to 0.97%. In the case of the AM05-VV10sol functional, there are several crystals for which significant errors in the lattice dimensions are found even though the calculated volume is in good agreement with experiment. For example, for crystal (3) the *a* and *c* lattice vectors are overestimated by 1.7 and 3.0%, respectively, while the *b* lattice vector is underestimated by −4.0%, causing the unit cell volume to be overestimated by only 0.5%.

For the lattice angles, the MAPE values for the top performing functionals are reported in Figure 7b. For these functionals, the calculated values of the α and γ lattice angles are within 0.27% of the experimental values, while the calculated values of the β lattice angle are within 0.8% of the experimental values.

The excellent performance of the optPBE-vdW method at predicting the crystal structures of the S26 set of high nitrogen content salts reinforces the results of ref 39, where it was found that this approach is remarkably successful for a wide range of solids including metals, ionic compounds, and insulators.

The comparison between theory and experiment presented above has been done using the calculated data for the potential energy minima whereas the experimental results include contributions due to vibrations. The vibrational degrees of freedom impact the structures in two distinct ways. First, even at 0 K, the experimentally determined lattice constants include the effects of vibrational anharmonicity, which causes the lattice constants to be larger than those associated with the potential energy minimum. Second, the experimental data have been collected in the range 90–295 K, with the great majority of the experimental data being measured at 200 K (see the footnote to Table 1). The finite temperature should act so as to cause an expansion of the lattice parameters. Theoretical analysis of such effects could be achieved by explicit calculation of the anharmonic vibrational frequencies or the use of molecular dynamic simulations in the NPT ensemble. Either of these two approaches would be very computationally demanding. For the

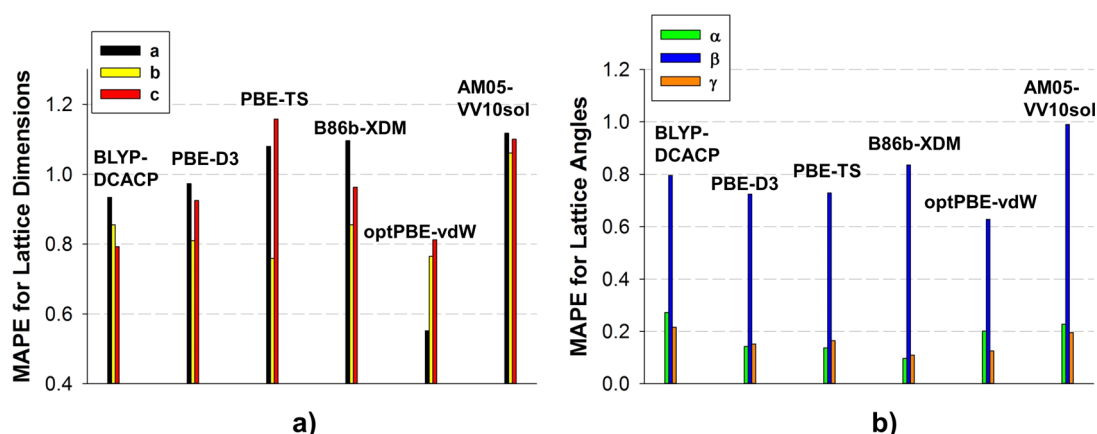


Figure 7. Comparison of the mean absolute percent errors (MAPE) of the calculated (a) unit cell lengths and (b) unit cell angles for the S26 set obtained using the top performance functionals: BLYP-DCACP, PBE-D3, PBE-TS, B86b-XDM, optPBE-vdW, and AM05-VV10sol.

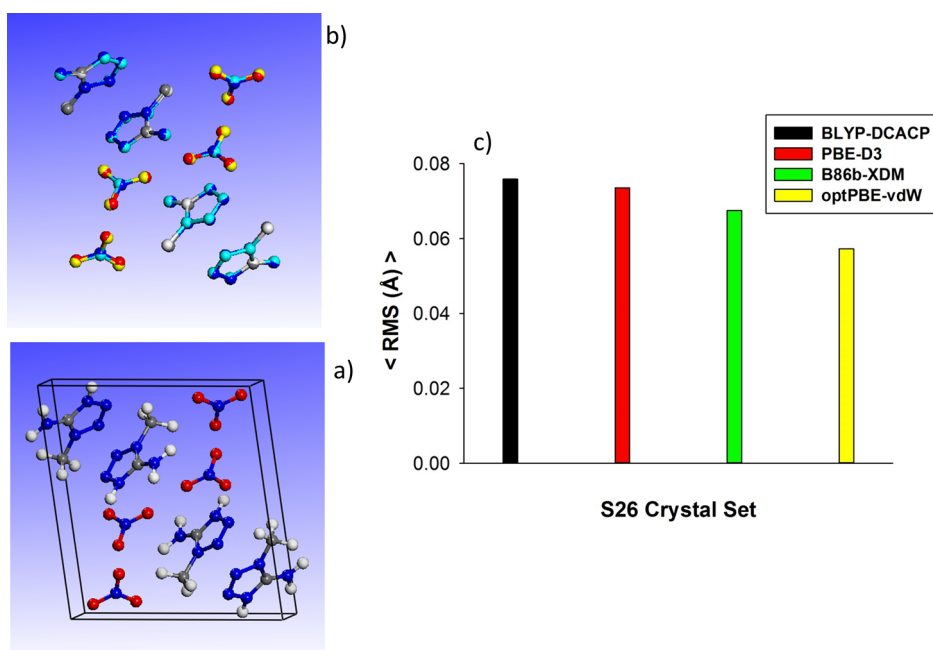


Figure 8. Pictorial views of the experimental structure of crystal 19 (a) and of the predicted structure of the same crystal superimposed onto its experimental counterpart (b). In the latter case, analysis was done only for the case of heavy atoms. The color scheme used to differentiate among the experimental and computed structures is as follows: dark and light gray for C, dark and light blue for N, and red and yellow for O atoms, respectively. (c) Comparison of the average RMS deviation of the predicted structures relative to experiment for the BLYP-DCACP, PBE-D3, B86b-XDM, and optPBE-vdW methods.

systems that comprise the S26 test set, we expect the volumes to be increased by at most 2% and, in general, by less than 1% due to the vibrational effects. Consequently, the findings of the current study are considered under the assumption that the vibrational effects do not affect dramatically the theoretical predictions, which ignore the contributions of vibrations and finite temperature.

In addition to the analysis of the lattice dimensions and unit cell volumes for the S26 crystal set, we have also determined the structural properties of each crystal and compared them with corresponding experimental data for the top performing theoretical methods. Specifically, we have analyzed the deviation of the specific arrangement of calculated cations and anions from the experimental data by using the method previously introduced by Kearsley.⁸⁶ Briefly, the method consists of two computational steps. In the first step, the

center of mass of the calculated unit cell is superimposed on its experimental counterpart such that the mass centers of the unit cells are at the system origin. In the second step, the entire set of molecules of the predicted crystal is rotated to minimize the sum of squared distances between the atoms in the predicted structure relative to the experimental counterpart. For illustration, a pictorial view of the rotated calculated structure superimposed to the corresponding experimental structure is shown in Figure 8b for crystal 19. For reference, we also indicate in Figure 8a the experimental structure of the same crystal. Once the structures have been superimposed, the root-mean-square (RMS) deviation of the atomic displacements of the predicted structure from the experimental structure was evaluated. This can be used to indicate the degree of similarity between the experimental and calculated crystal structures being compared. We note that due to the difficulties in locating

the H atoms in the experimental structures as determined by X-ray diffraction, we included only the heavy atoms (see Figure 8b) in the comparison procedure. Additionally, for supercells that contain more than one unit cell, atomic positions in the unit cell were averaged over all the unit cells of the supercell prior to comparison with the experimental structure.

The RMS deviations for each individual crystal in the S26 set is provided in Supporting Information Table S8 for the case of the top four best performing methods identified based on an analysis of crystallographic parameters, namely BLYP-DCACP, PBE-D3, B86b-XDM, and optPBE-vdW. The data obtained demonstrate that overall, for the entire set of values, relatively small deviations from the experimental data exist with RMS deviations ranging from 0.022 to 0.151 Å. The average RMS deviations for the S26 determined using the four methods indicated above are given in Figure 8b. It can be seen that the best agreement with experiment is obtained with the optPBE-vdW method followed closely by B86b-XDM, with BLYP-DCACP and PBE-D3 performing slightly poorer. The best performance obtained for the optPBE-vdW method with an average RMS deviation of 0.057 Å reinforces the results obtained previously for the lattice dimensions and angles (see Figure 7a and b) where this method was found to be the most accurate.

Beside the unit cell crystallographic and structural data another important metric considered is the cohesive energy. The cohesive energies were calculated for the S26 test set in the case of the BLYP-DCACP, PBE-D3, PBE-TS, and optPBE-vdW functionals, and the corresponding results are indicated in Supporting Information Figure S11. These have been determined by subtracting from the total energy of the supercell the sum of energies of isolated ions (and of the isolated neutral molecules when present) and dividing by the corresponding formula units. For the plane-wave codes, evaluation of the energies of the isolated ions was done using cubic unit cells with inclusion of dipole and quadrupole corrections. Using the optimized geometries of the crystal supercells and of the isolated ionic species, we have also evaluated the “dispersion” corrections to the cohesive energies and report the results in Supporting Information Figure S12.

Analysis of the data in Supporting Information Figure S11 indicates that cohesive energies can be grouped broadly into two groups, one with energies around 6.5 eV corresponding to systems with single charged ions and the other containing either double charged ions or a mixture of single and double charged ions with cohesive energies in excess of 15 eV. For the entire S26 set, it is observed that there is a small but systematic increase of cohesive energies when going from BLYP-DCACP to PBE-D3 and further to PBE-TS and optPBE-vdW. However, no definite answer about the level of accuracy provided by these functionals can be provided due to the lack of experimental measurements of the lattice energies for the S26 set.

From the data in Supporting Information Figure S12 it can be seen that the “dispersion” corrections are as large as 45% of the values of the net cohesive energies. These contributions decrease in magnitude from optPBE-vdW to DCACP-BLYP, and to the PBE-TS and PBE-D3 functionals. We note that these differences are not unexpected given the fact that some of the procedures are effectively correcting (at least in the overlap region) for deficiencies in the functionals other than neglect of long-range dispersion.

4. CONCLUSIONS

DFT calculations using uncorrected and dispersion-corrected functionals have been used to calculate the crystallographic lattice parameters for a set of 26 ionic high nitrogen content compounds. The main objective of this study was to screen different DFT methods which incorporate dispersion interactions and to identify those functionals that are capable of predicting the unit cell volumes within a target error range of less than 3%, a value which is a required threshold for accurate predictions of energetic materials formulations. In addition, we examined the performance of the various DFT methods at predicting the individual lattice dimensions and lattice angles. The main findings are

- (1) For the set of 19 combinations of different functionals and dispersion-correction schemes considered, the best agreement of the calculated lattice parameters and unit cell volumes with experiment is obtained using the optPBE-vdW functional of Klimeš et al.³⁸ With this functional, the calculated unit cell volumes for all members of the S26 set of crystals are within 3% of the experimental values and the individual lattice dimensions were predicted with a MAPE $\leq 0.8\%$. Additionally, a high degree of similarity with experimental structures is obtained in this case with an average RMS deviation of only 0.057 Å. The AM05-VV10sol functional also predicts unit cell volumes of the S26 set within the target error but at the expense of slightly less accurate predictions of the individual lattice dimensions (MAPE $\leq 1.1\%$)
- (2) With one exception, the BLYP-DCACP functional also predicts the unit cell volumes of the S26 set to within the specified target error of $\pm 3\%$. However, the use of the DCACP method as implemented in the CP2K code requires plane-wave cutoff energies for the density expansion of at least 2000 Ry to obtain converged structures, which makes this approach very computationally demanding.
- (3) The PBE-D3 and B86b-XDM methods are also quite successful at predicting the unit cell volumes and lattice constants and, given their computational speed, should prove useful in screening large numbers of candidates for crystal structures.
- (4) All of the functionals in the “best performing” list allow for dispersion corrections that depend on the chemical environment. Although the focus of this work was on the prediction of the crystallographic structures and cohesive energies of the S26 set of crystals, it is expected that these functionals would also prove to be viable for predicting other crystal properties.

■ ASSOCIATED CONTENT

Supporting Information

Schemes S1 and S2: list of anion–cation pairs for the C–N–H and C–N–O–H ionic salts investigated in this study. Tables S3 and S4: list of the supercells used in the calculations with CP2K and the list of Monkhorst Pack grids used in VASP and Quantum Espresso calculations to investigate the S26 set of high nitrogen crystals. Tables S5, S6, and S7: corresponding mean and mean percent errors, mean absolute and mean absolute percent errors, and the root-mean-square deviations of the unit cell volumes, lattice dimensions and lattice angles, respectively. Table S8: RMS deviations for S26 set from

experiment. Figure S9: variation of the unit cell volume with the cutoff energy used in B86b-XDM calculations for crystals (1) and (16). Figure S10: comparison of the unit cell volumes obtained using the PBE-D3 method as implemented in the VASP and CP2K codes. Figures S11 and S12: calculated cohesive energies for the S26 set and of the “dispersion” contributions to the cohesive energies determined using different methods, respectively. This material is available free of charge via the Internet at <http://pubs.acs.org>.

AUTHOR INFORMATION

Corresponding Author

*E-mail: edward.f.byrd2.civ@mail.mil.

Notes

The authors declare no competing financial interest.

ACKNOWLEDGMENTS

We acknowledge with thanks a supercomputing challenge grant at several DOD Supercomputing Resource Centers (DSRCs). Discussions with Dr. Tomas Bučko (Comenius University), Dr. Fabien Tran (Vienna University of Technology), and Dr. Alberto Otero de la Roza (University of California, Merced) on implementation of dispersion interactions in VASP, CP2K, and Quantum Espresso codes are gratefully acknowledged. K.D.J. acknowledges support from NSF through grant number CHE-1362334.

REFERENCES

- (1) Byrd, E. F. C.; Scuseria, G. E.; Chabalowski, C. F. An Ab Initio Study of Solid Nitromethane, HMX, RDX, and CL20: Successes and Failures of DFT. *J. Phys. Chem. B* **2004**, *108*, 13100–13106.
- (2) Kohn, W.; Sham, L. J. Self-Consistent Equations Including Exchange and Correlation Effects. *Phys. Rev.* **1965**, *140*, A1133–A1138.
- (3) Hohenberg, P.; Kohn, W. Inhomogeneous Electron Gas. *Phys. Rev. B* **1964**, *136*, B864–B871.
- (4) Byrd, E. F. C.; Rice, B. M. Ab Initio Study of Compressed 1,3,5,7-Tetranitro-1,3,5,7-Tetraazacyclooctane (HMX), Cyclotrimethylenetrinitramine (RDX), 2,4,6,8,10,12-Hexanitrohexaazaisowurztane (CL-20), 2,4,6-Trinitro-1,3,5-Benzenetriamine (TATB), and Pentaerythritol Tetranitrate (PETN). *J. Phys. Chem. C* **2007**, *111*, 2787–2796.
- (5) Grimme, S. Density Functional Theory with London Dispersion Corrections. *WIREs Comput. Mol. Sci.* **2011**, *1*, 211–228.
- (6) Klimeš, J.; Michaelides, A. Perspective: Advances and Challenges in Treating van Der Waals Dispersion Forces in Density Functional Theory. *J. Chem. Phys.* **2012**, *137*, 120901.
- (7) Otero-de-la-Roza, A.; Johnson, E. R. A Benchmark for Non-Covalent Interactions in Solids. *J. Chem. Phys.* **2012**, *137*, 054103.
- (8) Tkatchenko, A.; Romaner, L.; Hofmann, O. T.; Zojer, E.; Ambrosch-Draxl, C.; Scheffler, M. van Der Waals Interactions between Organic Adsorbates and at Organic/Inorganic Interfaces. *MRS Bull.* **2010**, *35*, 435–442.
- (9) von Lilienfeld, O. A.; Tavernelli, I.; Rothlisberger, U.; Sebastiani, D. Optimization of Effective Atom Centered Potentials for London Dispersion Forces in Density Functional Theory. *Phys. Rev. Lett.* **2004**, *93*, 153004.
- (10) Balu, R.; Byrd, E. F. C.; Rice, B. M. Assessment of Dispersion Corrected Atom Centered Pseudopotentials: Application to Energetic Molecular Crystals. *J. Phys. Chem. B* **2011**, *115*, 803–810.
- (11) Zhao, Y.; Truhlar, D. G. Density Functionals for Noncovalent Interaction Energies of Biological Importance. *J. Chem. Theory. Comput.* **2007**, *3*, 289–300.
- (12) Zhao, Y.; Truhlar, D. G. The M06 Suite of Density Functionals for Main Group Thermochemistry, Thermochemical Kinetics, Non-covalent Interactions, Excited States, and Transition Elements: Two New Functionals and Systematic Testing of Four M06-Class Functionals and 12 Other Functionals. *Theor. Chem. Acc.* **2008**, *120*, 215–241.
- (13) Karalti, O.; Su, X. G.; Al-Saidi, W. A.; Jordan, K. D. Correcting Density Functionals for Dispersion Interactions Using Pseudopotentials. *Chem. Phys. Lett.* **2014**, *591*, 133–136.
- (14) Grimme, S. Semiempirical GGA-Type Density Functional Constructed with a Long-Range Dispersion Correction. *J. Comput. Chem.* **2006**, *27*, 1787–1799.
- (15) Risthaus, T.; Grimme, S. Benchmarking of London Dispersion-Accounting Density Functional Theory Methods on Very Large Molecular Complexes. *J. Chem. Theory. Comput.* **2013**, *9*, 1580–1591.
- (16) Bucko, T.; Hafner, J.; Lebegue, S.; Angyan, J. G. Improved Description of the Structure of Molecular and Layered Crystals: Ab Initio DFT Calculations with van Der Waals Corrections. *J. Phys. Chem. A* **2010**, *114*, 11814–11824.
- (17) Reckien, W.; Janetzko, F.; Peintinger, M. F.; Bredow, T. Implementation of Empirical Dispersion Corrections to Density Functional Theory for Periodic Systems. *J. Comput. Chem.* **2012**, *33*, 2023–2031.
- (18) Sorescu, D. C.; Rice, B. M. Theoretical Predictions of Energetic Molecular Crystals at Ambient and Hydrostatic Compression Conditions Using Dispersion Corrections to Conventional Density Functionals (DFT-D). *J. Phys. Chem. C* **2010**, *114*, 6734–6748.
- (19) Grimme, S.; Antony, J.; Ehrlich, S.; Krieg, H. A Consistent and Accurate Ab Initio Parametrization of Density Functional Dispersion Correction (DFT-D) for the 94 Elements H–Pu. *J. Chem. Phys.* **2010**, *132*, 154104–154119.
- (20) Tkatchenko, A.; Scheffler, M. Accurate Molecular Van Der Waals Interactions from Ground-State Electron Density and Free-Atom Reference Data. *Phys. Rev. Lett.* **2009**, *102*, 073005.
- (21) Becke, A. D.; Johnson, E. R. A Density-Functional Model of the Dispersion Interaction. *J. Chem. Phys.* **2005**, *123*, 154101.
- (22) Becke, A. D.; Johnson, E. R. Exchange-Hole Dipole Moment and the Dispersion Interaction. *J. Chem. Phys.* **2005**, *122*, 154104.
- (23) Becke, A. D.; Johnson, E. R. Exchange-Hole Dipole Moment and the Dispersion Interaction Revisited. *J. Chem. Phys.* **2007**, *127*, 154108.
- (24) Chai, J.-D.; Head-Gordon, M. Long-Range Corrected Hybrid Density Functionals with Damped Atom–Atom Dispersion Corrections. *Phys. Chem. Chem. Phys.* **2008**, *10*, 6615–6620.
- (25) Brandenburg, J.; Grimme, S. Dispersion Corrected Hartree–Fock and Density Functional Theory for Organic Crystal Structure Prediction. *Top. Curr. Chem.* **2013**, *345*, 1–23.
- (26) Hirshfeld, F. L. Bonded-Atom Fragments for Describing Molecular Charge-Densities. *Theor. Chim. Acta* **1977**, *44*, 129–138.
- (27) Tkatchenko, A.; DiStasio, R. A., Jr.; Car, R.; Scheffler, M. Accurate and Efficient Method for Many-Body van Der Waals Interactions. *Phys. Rev. Lett.* **2012**, *108*, 236402.
- (28) Otero-de-la-Roza, A.; Johnson, E. R. van Der Waals Interactions in Solids Using the Exchange-Hole Dipole Moment Model. *J. Chem. Phys.* **2012**, *136*, 174109.
- (29) Johnson, E. R.; Becke, A. D. A Post-Hartree–Fock Model of Intermolecular Interactions. *J. Chem. Phys.* **2005**, *123*, 024101.
- (30) Becke, A. D. On the Large-Gradient Behavior of the Density Functional Exchange Energy. *J. Chem. Phys.* **1986**, *85*, 7184–7187.
- (31) Perdew, J. P.; Yue, W. Accurate and Simple Density Functional for the Electronic Exchange Energy: Generalized Gradient Approximation. *Phys. Rev. B* **1986**, *33*, 8800–8802.
- (32) Grimme, S.; Ehrlich, S.; Goerigk, L. Effect of the Damping Function in Dispersion Corrected Density Functional Theory. *J. Comput. Chem.* **2011**, *32*, 1456–1465.
- (33) Dion, M.; Rydberg, H.; Schroder, E.; Langreth, D. C.; Lundqvist, B. I. van Der Waals Density Functional for General Geometries. *Phys. Rev. Lett.* **2004**, *92*, 246401.
- (34) Murray, E. D.; Lee, K.; Langreth, D. C. Investigation of Exchange Energy Density Functional Accuracy for Interacting Molecules. *J. Chem. Theory. Comput.* **2009**, *5*, 2754–2762.

- (35) Lee, K.; Murray, E. D.; Kong, L.; Lundqvist, B. I.; Langreth, D. C. Higher-Accuracy van Der Waals Density Functional. *Phys. Rev. B* **2010**, *82*, 081101.
- (36) Vydrov, O. A.; Van Voorhis, T. Nonlocal van Der Waals Density Functional Made Simple. *Phys. Rev. Lett.* **2009**, *103*, 063004.
- (37) Vydrov, O. A.; Van Voorhis, T. Dispersion Interactions from a Local Polarizability Model. *Phys. Rev. A* **2010**, *81*, 062708.
- (38) Klimeš, J.; Bowler, D. R.; Michaelides, A. Chemical Accuracy for the van Der Waals Density Functional. *J. Phys.: Condens. Matter* **2010**, *22*, 022201.
- (39) Klimeš, J.; Bowler, D. R.; Michaelides, A. Van Der Waals Density Functionals Applied to Solids. *Phys. Rev. B* **2011**, *83*, 195131.
- (40) Vydrov, O. A.; Van Voorhis, T. Nonlocal van Der Waals Density Functional: The Simpler the Better. *J. Chem. Phys.* **2010**, *133*, 244103.
- (41) Tran, F.; Hutter, J. Nonlocal van Der Waals Functionals: The Case of Rare-Gas Dimers and Solids. *J. Chem. Phys.* **2013**, *138*, 204103.
- (42) Björkman, T.; Gulans, A.; Krashennnikov, A. V.; Nieminen, R. M. Are We van Der Waals Ready? *J. Phys.: Condens. Matter* **2012**, *24*, 424218.
- (43) Björkman, T. van Der Waals Density Functional for Solids. *Phys. Rev. B* **2012**, *86*, 165109.
- (44) Armiento, R.; Mattsson, A. E. Functional Designed to Include Surface Effects in Self-Consistent Density Functional Theory. *Phys. Rev. B* **2005**, *72*, 085108.
- (45) Klapoetke, T. M.; Stierstorfer, J. The Cn_7^- Anion. *J. Am. Chem. Soc.* **2009**, *131*, 1122–1134.
- (46) Klapoetke, T. M.; Petermayer, C.; Piercey, D. G.; Stierstorfer, J. 1,3-Bis(Nitroimido)-1,2,3-Triazole Anion, the N-Nitroimide Moiety, and the Strategy of Alternating Positive and Negative Charges in the Design of Energetic Materials. *J. Am. Chem. Soc.* **2012**, *134*, 20827–20836.
- (47) Gao, H.; Shreeve, J. n. M. Azole-Based Energetic Salts. *Chem. Rev.* **2011**, *111*, 7377–7436.
- (48) Zhang, Q.; Shreeve, J. n. M. Growing Catenated Nitrogen Atom Chains. *Angew. Chem., Int. Ed.* **2013**, *52*, 8792–8794.
- (49) Klapoetke, T. M.; Nöth, H.; Schwenk-Kircher, H.; Walther, W.-H.; Holl, G. Synthesis and X-ray Structure of 1,1-Dimethylhydrazinium Azide. *Polyhedron* **1999**, *18*, 717–719.
- (50) Haberer, T.; Hammerl, A.; Holl, G.; Klapoetke, T. M.; Knizek, J.; Nöth, H. Synthesis and X-ray Structure Determination of *tert*-Butylhydrazinium Azide and N,N,N-Trimethylhydrazinium Azide. *Eur. J. Inorg. Chem.* **1999**, *1999*, 849–852.
- (51) Hammerl, A.; Holl, G.; Hübler, K.; Kaiser, M.; Klapoetke, T. M.; Mayer, P. Methylated Derivatives of Hydrazinium Azide. *Eur. J. Inorg. Chem.* **2001**, *2001*, 755–760.
- (52) Hammerl, A.; Holl, G.; Kaiser, M.; Klapoetke, T. M.; Mayer, P.; Nöth, H.; Warchhold, M. New Hydrazinium Azide Compounds. *Z. Anorg. Allg. Chem.* **2001**, *627*, 1477–1482.
- (53) Crawford, M.-J.; Karaghiosoff, K.; Klapoetke, T. M.; Martin, F. A. Synthesis and Characterization of 4,5-Dicyano-2h-1,2,3-Triazole and Its Sodium, Ammonium, and Guanidinium Salts. *Inorg. Chem.* **2009**, *48*, 1731–1743.
- (54) Hammerl, A.; Holl, G.; Kaiser, M.; Klapoetke, T. M.; Mayer, P.; Nöth, H.; Piotrowski, H.; Suter, M. New Hydrazinium Salts of 5,5'-Azotetrazolate. *Z. Naturforsch., B: Chem. Sci.* **2001**, *56*, 857–870.
- (55) Hammerl, A.; Holl, G.; Kaiser, M.; Klapoetke, T. M.; Mayer, P.; Piotrowski, H.; Vogt, M. Methylated Ammonium and Hydrazinium Salts of 5,5'-Azotetrazolate. *Z. Naturforsch., B: Chem. Sci.* **2001**, *56*, 847–856.
- (56) Klapoetke, T. M.; Sabaté, C. M. Nitrogen-Rich Tetrazolium Azotetrazolate Salts: A New Family of Insensitive Energetic Materials. *Chem. Mater.* **2008**, *20*, 1750–1763.
- (57) Hammerl, A.; Hiskey, M. A.; Holl, G.; Klapoetke, T. M.; Polborn, K.; Stierstorfer, R.; Weigand, J. J. Azidoformamidinium and Guanidinium 5,5'-Azotetrazolate Salts. *Chem. Mater.* **2005**, *17*, 3784–3793.
- (58) Stierstorfer, J. *Chemistry of Bistetrazolylamines*. Diploma Thesis, Ludwig-Maximilian University of Munich, Munich, 2005.
- (59) Bonn, O. d.; Hammerl, A.; Klapoetke, T. M.; Mayer, P.; Piotrowski, H.; Zewen, H. Plume Deposits from Bipropellant Rocket Engines: Methylhydrazinium Nitrate and N,N-Dimethylhydrazinium Nitrate. *Z. Anorg. Allg. Chem.* **2001**, *627*, 2011–2015.
- (60) von Denffer, M.; Klapoetke, T. M.; Kramer, G.; Spiess, G.; Welch, J. M.; Heeb, G. Improved Synthesis and X-ray Structure of 5-Aminotetrazolium Nitrate. *Propellants Explosives Pyrotechnics* **2005**, *30*, 191–195.
- (61) Karaghiosoff, K.; Klapoetke, T. M.; Mayer, P.; Sabaté, C. M.; Penger, A.; Welch, J. M. Salts of Methylated 5-Aminotetrazoles with Energetic Anions. *Inorg. Chem.* **2008**, *47*, 1007–1019.
- (62) Klapoetke, T. M.; Miró Sabaté, C. 1,2,4-Triazolium and Tetrazolium Picrate Salts: “On the Way” from Nitroaromatic to Azole-Based Energetic Materials. *Eur. J. Inorg. Chem.* **2008**, 5350–5366.
- (63) Gálvez-Ruiz, J. C.; Holl, G.; Karaghiosoff, K.; Klapoetke, T. M.; Löhnwitz, K.; Mayer, P.; Nöth, H.; Polborn, K.; Rohbogner, C. J.; Suter, M.; Weigand, J. J. Derivatives of 1,5-Diamino-1h-Tetrazole: A New Family of Energetic Heterocyclic-Based Salts. *Inorg. Chem.* **2005**, *44*, 5192–5192.
- (64) Göbel, M.; Klapoetke, T. M. Potassium-, Ammonium-, Hydrazinium-, Guanidinium-, Aminoguanidinium-, Diaminoguanidinium-, Triaminoguanidinium-, and Melaminiumnitroformate- Synthesis, Characterization, and Energetic Properties. *Z. Anorg. Allg. Chem.* **2007**, *633*, 1006–1017.
- (65) Guo, Y.; Gao, H.; Twamley, B.; Shreeve, J. M. Energetic Nitrogen Rich Salts of N,N-bis 1(2)H-tetrazol-5-yl Amine. *Adv. Mater.* **2007**, *19*, 2884–2888.
- (66) VandeVondele, J.; Krack, M.; Mohamed, F.; Parrinello, M.; Chassaing, T.; Hutter, J. Quickstep: Fast and Accurate Density Functional Calculations Using a Mixed Gaussian and Plane Waves Approach. *Comput. Phys. Commun.* **2005**, *167*, 103–128.
- (67) CP2K. Version 2.5. CP2K is Freely Available from www.cp2k.org.
- (68) Kresse, G.; Furthmüller, J. Efficiency of Ab-Initio Total Energy Calculations for Metals and Semiconductors Using a Plane-Wave Basis Set. *Comput. Mater. Sci.* **1996**, *6*, 15–50.
- (69) Kresse, G.; Furthmüller, J. Efficient Iterative Schemes for Ab Initio Total-Energy Calculations Using a Plane-Wave Basis Set. *Phys. Rev. B* **1996**, *54*, 11169–11186.
- (70) Giannozzi, P.; Baroni, S.; Bonini, N.; Calandra, M.; Car, R.; Cavazzoni, C.; Ceresoli, D.; Chiarotti, G. L.; Cococcioni, M.; Dabo, I.; Dal Corso, A.; de Gironcoli, S.; Fabris, S.; Fratesi, G.; Gebauer, R.; Gerstmann, U.; Gougoussis, C.; Kokalj, A.; Lazzeri, M.; Martin-Samos, L.; Marzari, N.; Mauri, F.; Mazzarello, R.; Paolini, S.; Pasquarello, A.; Paulatto, L.; Sbraccia, C.; Scandolo, S.; Sclauzero, G.; Seitsonen, A. P.; Smogunov, A.; Umari, P.; Wentzcovitch, R. M. Quantum Espresso: A Modular and Open-Source Software Project for Quantum Simulations of Materials. *J. Phys.: Condens. Matter* **2009**, *21*, 395502.
- (71) Lippert, G.; Hutter, J.; Parrinello, M. A Hybrid Gaussian and Plane Wave Density Functional Scheme. *Mol. Phys.* **1997**, *92*, 477–487.
- (72) Perdew, J. P.; Burke, K.; Ernzerhof, M. Generalized Gradient Approximation Made Simple. *Phys. Rev. Lett.* **1996**, *77*, 3865–3868.
- (73) Becke, A. D. Density-Functional Exchange-Energy Approximation with Correct Asymptotic-Behavior. *Phys. Rev. A* **1988**, *38*, 3098–3100.
- (74) Lee, C. T.; Yang, W. T.; Parr, R. G. Development of the Colle-Salvetti Correlation-Energy Formula into a Functional of the Electron Density. *Phys. Rev. B* **1988**, *37*, 785–789.
- (75) Zhang, Y.; Yang, W. Comment on “Generalized Gradient Approximation Made Simple”. *Phys. Rev. Lett.* **1998**, *80*, 890–890.
- (76) Bučko, T.; Lebègue, S.; Hafner, J.; Ángyán, J. G. Tkatchenko–Scheffler van Der Waals Correction Method with and without Self-Consistent Screening Applied to Solids. *Phys. Rev. B* **2013**, *87*, 064110.
- (77) Marques, M. A. L.; Oliveira, M. J. T.; Burnus, T. Libxc: A Library of Exchange and Correlation Functionals for Density Functional Theory. *Comput. Phys. Commun.* **2012**, *183*, 2272–2281.

- (78) Sabatini, R.; Gorni, T.; de Gironcoli, S. Nonlocal van Der Waals Density Functional Made Simple and Efficient. *Phys. Rev. B* **2013**, *87*, 041108.
- (79) Román-Pérez, G.; Soler, J. M. Efficient Implementation of a van Der Waals Density Functional: Application to Double-Wall Carbon Nanotubes. *Phys. Rev. Lett.* **2009**, *103*, 096102.
- (80) VandeVondele, J.; Hutter, J. Gaussian Basis Sets for Accurate Calculations on Molecular Systems in Gas and Condensed Phases. *J. Chem. Phys.* **2007**, *127*, 11405.
- (81) Goedecker, S.; Teter, M.; Hutter, J. Separable Dual-Space Gaussian Pseudopotentials. *Phys. Rev. B* **1996**, *54*, 1703–1710.
- (82) Blöchl, P. E. Projector Augmented-Wave Method. *Phys. Rev. B* **1994**, *50*, 17953.
- (83) Kresse, G.; Joubert, D. From Ultrasoft Pseudopotentials to the Projector Augmented-Wave Method. *Phys. Rev. B* **1999**, *59*, 1758–1775.
- (84) Monkhorst, H. J.; Pack, J. D. Special Points for Brillouin-Zone Integrations. *Phys. Rev. B* **1976**, *13*, 5188–5192.
- (85) Otero-de-la-Roza, A.; Johnson, E. R. Non-Covalent Interactions and Thermochemistry Using XDM-Corrected Hybrid and Range-Separated Hybrid Density Functionals. *J. Chem. Phys.* **2013**, *138*, 204109.
- (86) Kearsley, S. K. On the Orthogonal Transformation Used for Structural Comparisons. *Acta Crystallogr. A* **1989**, *45*, 208–210.